90

Egypt. J. Chem. **Vol. 65,** No. SI:13B pp. 949 - 957 (2022)

Egyptian Journal of Chemistry

Effect of increasing Fe-concentrations on ZnO thin film deposited by sol-gel spin coater.

Nora Y. Elsheikh [1], Inas K. Battisha[*2] Ahmed Abo Arais[1], M.S. Shams[1]

1 Menoufia University, Faculty of Electronic Engineering, Physics and Mathematical Engineering Department, 32952 Menouf, Egypt.

2 National Research Centre, Solid state physics department, Physics Research Institute, Dokki, Giza, Egypt, Affiliation ID: 60014618

Abstract

To produce transparent thin films of undoped and Fe-loaded zinc oxide (ZnO) referred to as ZTF, Z (15-30 %F), the current study utilizes a modified sol-gel spin coating method (Zn-Fe). Both undoped and Fe-loaded ZnO thin films were annealed at 500^0C for 2 hours. The morphologies and the structural characteristics of pure and doped ZnO thin films were studied. The structure of the resulting films was investigated using X-ray diffraction (XRD) spectra, revealing good crystal quality and a pure hexagonal wurtzite ZnO structure free of Fe-associated phases. The crystallite size of undoped ZnO thin film is 10.47 nm, and it decreases when the Fe content is increased to 25 mol. %, then it returns to increase at 30 mol. %, giving the following values 10.37, 9.66, 8.26, and 15.59 nm, respectively. Plane images were taken with a field emission scanning electron microscope (FESEM) revealing spherical particles and smooth surface shapes in the ZnO thin film, whilst Fe-loaded ZnO films have a uniform and compact morphology. The Laser-based Raman micro-spectroscopy presents the homogenous distribution of the iron oxide. The optical properties of thin films, such as transmittance (T %) and the absorption coefficient obtained from the absorbance spectrum were determined using UV/vis spectroscopy. The T% of ZTF film exhibited an average value of nearly 97% and reduced when the Fe concentrations were increased. ZTF, Z15FTF, Z20FTF, Z25FTF, and Z30FTF have energy band gaps of 3.138, 3.234, 3.240, 3.242, 2.936eV, respectively.

Keywords : Sol-Gel ; Thin film ; ZnO ; iron ; 3-D laser Raman.

1. Introduction

The (ZTF) is a high transparent conducting oxide (TCO) material [1] in the near-infrared and visible regions. It has chemical stability in hydrogen plasma and great mechanical too. The (ZTF) is an interesting material for electronic and optoelectronic applications such as heat mirrors, gas sensors, solar cells, surface acoustic waves, liquid crystal display devices, and others [2-7], thanks to these properties. ZnO thin films can be also utilized in biosensors and integrated optics. Magnetron sputtering [8], electrodeposition [10], spray pyrolysis [9], sol-gel dip and spin coating techniques [11], pulsed laser deposition [12], thermal evaporation deposition, chemical bath deposition, SILAR [14], and chemical vapor deposition [13], can all be used to synthesize ZTF. The spin coater sol-gel is used as a deposition method in the present work, which has a higher usage rate due to its relatively low temperature, the ease of fabricating the sample, the simplicity of the system and operation, and the ease of

doping by mixing the precursors in the proper ratio [15]. This paper introduced the optical and structural studies of ZTF and ZTF (15-30 mol. %Fe) created utilizing the sol-gel spin coating method. We will discuss how the concentration of precursors affects optical transmittance, optical absorption, and optical band gap.

2. Experiments and Characterization

2.1. Experiments

Nano-structure Wurtzite hexagonal pure ZnO thin films were formed using a homemade sol-gel spin coating process and deposited on a pre-cleaned substrate. They were doped with varying amounts of iron Fe^{3+} ions at (0.0, 15, 20, 25, and 30 mol.% Fe). These films are referred to ZTF, Z15FTF, Z20FTF, Z25FTF, and Z30FTF, respectively. The substrate must be thoroughly cleaned prior to the ZnO thin film being deposited. The substrates were bathed in ethanol for 20 minutes. Then, cleaned in an ultrasonic device for another 20 minutes. So, bathed in bi-distilled water

_____

for another 20 minutes before being dried using nitrogen-compressed air. This method leaves the substrate surface clean and ready for subsequent treatments by removing unwanted materials and dust. Numerous precursors and solvents were used for the creation of the required solution. At room temperature, zinc acetate dehydrate ($ZnCH_3COO)_2.2H_2O$) was dissolved at room temperature in a mixed solution of mono-ethanolamine ($NH_2CH_2CH_2OH$) (MEA) and 2-methoxy ethanol, where the molar ratio of MEA to zinc acetate was 1:1. By adding iron nitrate with molar ratios of 15, 20, 25, and 30 mol.% to the initial solution, the Fe^{+3} ions were generated in the process. This mixture was brought to 60°C and stirred for two hours until reached homogenous and clear shape. The final phase can be obtained by ageing for 24 hours at room temperature. The homogeneously mixed solutions were spun for 30 seconds on glass substrate at 3000 rpm, using the spin coater. The coating procedure was carried out repeatedly ten times to obtain ten successfully layers. The film was then annealed for two hours at 500 °C in the air.

2.2. characterization

To determine the phases of the produced and calcinated films, we used X-ray diffraction. employing a monochromatic Cu-Kα1 (λ=1.5406 Å) and a 40 kV-30 mA Philips X-ray diffractometer. The substrates were scanned at a rate of 2°/min from 25 to 75°. Scherrer's equation (1) provides a calculation of the crystalline size (D) [16]

$$D = K\lambda / \beta \cos\theta \qquad (1)$$

where K is the Scherer constant, K= (0.89), β is the peak full width at half maximum (FWHM) (in radians) intensity, λ is the wavelength, and θ is the diffracted angle.

The dislocation density (δ) and the strain function (ε) were determined according to equations (2 and 3) and shown in Table 2.

$$\delta = \frac{1}{D^2} \qquad (2)$$

$$\varepsilon = \frac{\beta \cos\theta}{4} \qquad (3)$$

The lattice constants (a and c) and the interplanar spacing d_{hkl} of ZnO NPs are computed from the lattice geometry equation as indicated below.

$$\lambda = 2d\sin\theta$$

$$\frac{1}{d^2} = \frac{4}{3} \cdot \frac{(h^2 + hk + k^2)}{a^2} + \frac{l^2}{c^2}$$

(010) and (002) reflections are applied to determine the lattice constants a and c, respectively.

$$a = \lambda/(3)^{1/2} \sin\theta_{010} \qquad (4)$$

And the lattice constant 'c' was assessed for the (002) plane by the equation

$$c = \lambda/ \sin\theta_{002} \qquad (5)$$

The unit cell volume (V) of a hexagonal system was calculated by the following equation:

$$V = 0.886 \times a^2 \times c \qquad (6)$$

Raman spectra characterization was achieved using the 514.5 nm lines from argon ion laser and examined using a Jobin Yvon T64000 spectrometer equipped with a charge-coupled device. An optical microscope was used to focus the light incident on a spot of about 2 μm in diameter on the sample. Unpolarized Raman spectra were achieved in backscattering geometry.

The microstructures of the produced samples were evaluated using a field emission scanning electron microscope (FESEM) (FESEM, Quanta FEG 250, FEI, USA). The FESEM offers images of the sample surface morphology that can be used to verify sample growth. The elemental chemical composition was verified using an energy dispersive x-ray spectrometer (EDS) coupled to a field emission scanning electron microscope.

The reflection spectra and optical transmission of the prepared films were obtained in the range of 200–2500 nm using a double-beam spectrophotometer (SP, V-570, JASCO, Japan) in conjunction with automatic computer data acquisition and photometric accuracy of +0.002 % absorbance and 0.30% transmittance.

3. Results and discussion

3.1. Structural analysis

Fig. 1 illustrates the ZTF, Z15FTF, Z20FTF, Z25FTF, and Z30FTF XRD charts. The wurtzite hexagonal phase structure is existing in the prepared samples. The synthesized materials' polycrystalline and efficient nature was confirmed by the appearance of prominent and clear peaks in all of the films. The pure and Fe-doped ZnO films showed diffraction peaks at $2\theta^0$ angles at 31.71°, 34.18°, 35.99°, 47.63°, 56.61°, 62.73°, and 68.07°, which are attributed to the following planes (100), (002), (101), (102), (110), (103)and (112) planes, respectively. The results are compatible with the literature(JCPDF card no 01-089-0510) with preferred principle orientation along the (101) plane. No extra peaks for Fe metal or FeO phases have appeared, Thus proving that the Fe dopant ought to be introduced as a substitutional atom into the lattice

_____

_____

of Zn–O. We noticed from Fig. 1 that by increasing the Fe dopant concentrations, all the peaks shifted to lower$2\theta^0$.
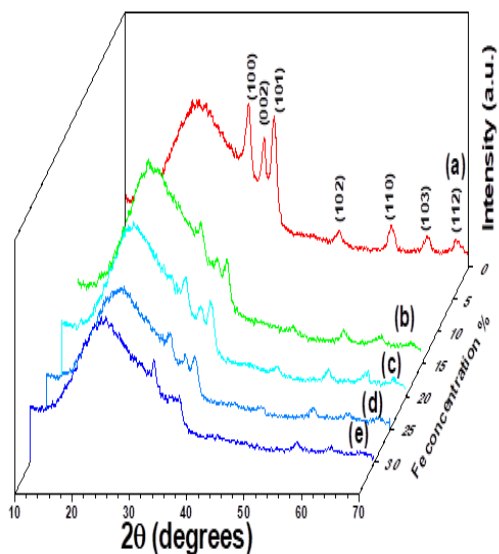

Fig. 1 The x-ray diffraction patterns for (a) ZTF, (b) Z15FTF, (c) Z20FTF, (d) Z25FTF and(e) Z30FTF, respectively sintered for 2 hours at 500

The calculated lattice parameters a and c for all samples by using equations (2-5) are tabulated in Table 1. Little shift values in both a and c were detected. In our sample, the c/a fraction gave values in the range between 1.595 and 1.610, which may appear the growth of oxygen on the interstitial locations and zinc vacancies(VZn). Fe is steadily in both valence states i.e., Fe^{2+} and Fe^{3+} states. If Fe is in Fe^{2+} (0.078 nm) state, the peak shifts to smaller angles attributable to its big ionic radii than Zn^{2+} (0.074nm). On the other hand, if it is in a Fe^{3+} (0.068nm) state, the peak will shift in the direction of a greater angle. So we believe that iron is in typically a 2+ state in our prepared samples. Despite this, the existence of a few contents of Fe^{3+} cannot be ignored without further explanations. As it is revealed in the XRD pattern, the intensity of the peaks was usually reduced by increasing Fe concentration, which shows the degradation of crystallinity, because the intensity is directly related to the atomic number of the elements. So when replacing the Zn (with atomic number AN=30) with the lower value of Fe (=26), the intensity of peaks decreases.

When Fe is added to the matrix, the specimens go from being ordered to being disordered, as shown in our results. Such little changes demonstrate that Zn has been replaced by Fe in the ZnO matrix, ensuring that Fe embedding does not affect the ZnO structure. The crystallite size values calculated from equation (1) and listed in Table 2 are equal to 10.47 nm for undoped ZnO, then decreased by increasing the Fe contents up to 25 mol.%, then it returns to increase at 30 mol.%, giving the following values 10.37,9.66,8.26 and 15.59 nm, respectively.

This reduction can be clarified by the lattice deformation [18], which is related to the reduction in nucleation and growth rate owing to the greater ionic radius of Fe^{2+} compared to Zn^{2+}. As well, the micro stress of the Fe-loaded sample rises with the doping amount, and the positive signs of strain values act for tensile strain. The raised strain is associated with a decrease in particle size, meaning that doping has an impact on ZnO crystal structure. The dislocation density (δ) is the number of dislocation lines per unit volume in the as-prepared films, which is found in its lowest value for Z30FTF compared to pure and other Fe-loaded ZnO films. At this doping concentration, a minimal value of δ reveals the presence of small defects in the deposited films and the creation of high-quality layers [19].

Table 1 The structural properties(a) ZTF, (b) Z15FTF, (c) Z20FTF, (d) Z25FTF and(e) Z30FTF, respectively, sintered for 2 hours at 500 ^{0}C.

	Sample names	symbols	a(Å)	c(Å)	c/a ratio	V(Å)^3
(a)	Pure ZnO	ZTF	3.253	5.208	1.6007	48.8528
(b)	0.15 Fe	Z15FTF	3.273	5.223	1.5958	49.5753
(c)	0.20 Fe	Z20FTF	3.270	5.223	1.5969	49.5062
(d)	0.25 Fe	Z25FTF	3.255	5.242	1.6103	49.2353
(e)	0.30 Fe	Z30FTF	3.245	5.187	1.5983	48.4226

Table 2 The crystallite size, Dislocation Density, and micro-strain of ZTF, Z15FTF, Z20FTF, Z25FTF, and Z30FTF samples, respectively, were sintered at 500^{0}C for 2 hours.

Fe dopant %	Crystallite Size(D) from XRD nm	Dislocation Density(δ) $*10^{-3}$ (nm)$^{-2}$	MicroStrain(ε)
0.0	10.47	9.123	0.00331
0.15	10.37	9.286	0.00334
0.20	9.66	10.726	0.00359
0.25	8.26	14.643	0.00419
0.30	15.59	4.111	0.00222

_____

_____

3.2. Raman analysis

The Raman equipment is an essential and flexible diagnostic tool analytical instrument for the crystallization, structural disorder, and imperfections in nano and microstructures. Raman spectra are employed to analyze the vibrational properties of the prepared films. The hexagonal wurtzite structure of ZnO nanostructures belongs to the P63mc space group.

only the optical phonons at Γ point to the Brillouin zone are included in first-order Raman scattering for the accurate ZnO crystal. Optical modes should be present in wurtzite ZnO, consistent with group theory, as shown in equation (7) [20,21].

$$\Gamma opt = A_1 + 2B_2 + E_1 + 2E_2 \qquad (7)$$

Whenever, both the E1 and A1 modes are two polar branches. For macroscopic electric fields associated with the LO phonons, these are split into transverse optical (TO) and longitudinal optical (LO) components with varying frequencies. B1 modes are referred to as "silent modes" because they are inactive in Raman spectra. A1, E_1, and E_2 modes are first-order Raman-active modes. Fig. 2 shows the 3D Raman spectra of pure and loaded with 25 mol.% of iron zinc oxide thin film. The fundamental phonon modes of hexagonal ZnO have been located at 94, 442, 528, and 562 cm^{-1}, it represents E_{2L}, E_{2H}, $A_1(LO)$ and$A_1(LO)/E_1(LO)$ respectively. The detected peaks at 777 and 1087 cm^{-1} are belonging to the glass substrate[22].

The E_{2H} mode has been decreased and broadened when increasing the Fe-dopant concentrations. As well, the $A_1(LO)/E_1(LO)$ polar mode at nearly 562 cm^{-1} has been presented for pure and Fe-doping causing this peak to be broadened and shifted to lower energy. The scattering contributions produced outside the Brillouin zone center are provided for all the shifting and broadening of phonon modes. The defect complexes of zinc interstitial and oxygen vacancy in the ZnO lattice are commonly represented by the $A_1(LO)/E_1(LO)$ phonon mode.
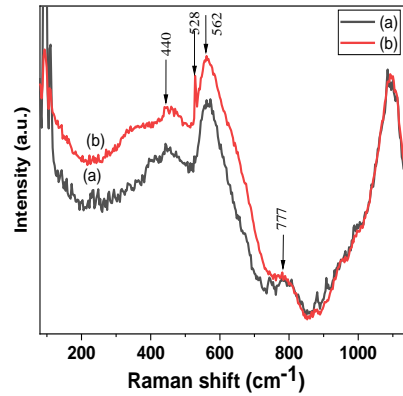

Fig.2 The Raman spectra of ZTF and Z25FTF samples, respectively, sintered for 2 hours at 500 °C.

3.3. Morphological analyses

The surface morphologies for the ZTF and Z25FTF sintered for 2 hours at 500 °C are shown in Fig. 3(a and b). The thickness of pure ZnO film is nearly 338 nm, measured by FESEM as shown in Fig. 3(c) .Doping with Fe ions causes a significant change in the surface morphology of both films. The ZTF morphology appears to be made of interconnected spherical particles with the existence of some pores. The mentioned pores are occupied a little for the Z25FTF sample.
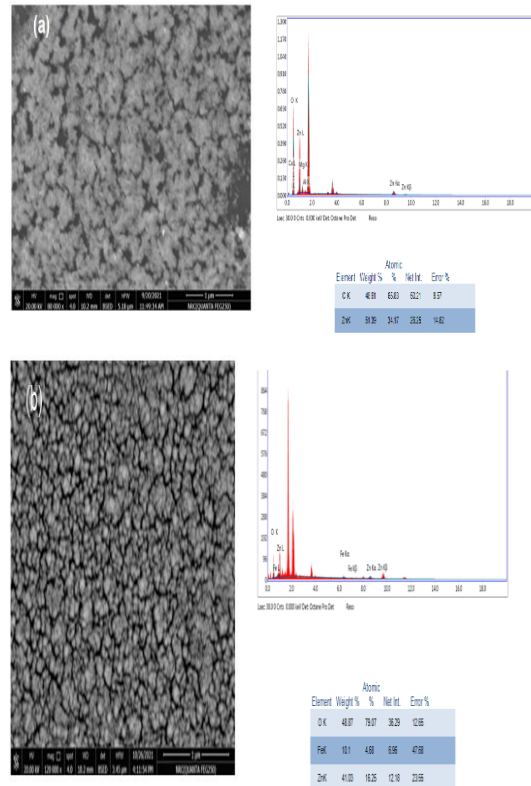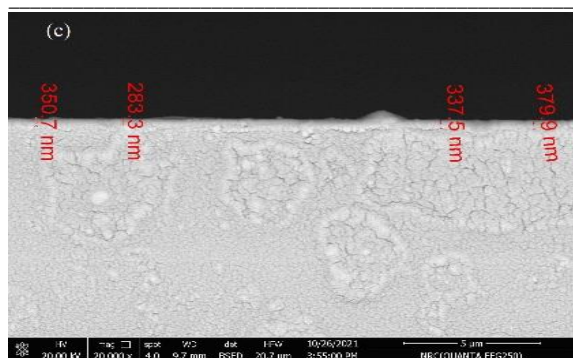
Fig. 3(a,b) The FESEM micrographs and EDX spectra of ZTF(a) and Z25FTF (b), respectively,cross-section view of pure film(c) , sintered for 2 hours at 500 ^{0}C.

3.4. Elemental studies

3.5. Optical properties

Fig. 4(a) displays the absorbance spectrum of ZTF, Z15FTF, Z20FTF, Z25FTF, and Z30FTF samples, which indicated that they have elevated UV absorbance values at wavelengths lower than 400 nm. The sharp absorption edge was observed around 354 nm, 354 nm, 356 nm, 298 nm, and 298 nm for ZTF, Z15FTF, Z20FTF, Z25FTF, and Z30FTF, respectively.

It is related to the direct transition of electrons between the edges of the valance and the conduction band. The transmittance and reflectance values were determined from the absorbance values utilizing the next relations in equations (8), (9) [24]:

$$T = 10^{-A} \tag{8}$$

Where T is Transmittance, A is Absorbance, and R is Reflectance.

$$R= 1-(A+T) \tag{9}$$

α is the absorption coefficient, which is given by, T % and the material thickness, d as presented in equation (10) [28];

$$\alpha = \frac{1}{d} \ln \frac{1}{T} \tag{10}$$

The energy band gap E_g is related to the absorption coefficient by this equation $(\alpha h\nu) = A (h\nu-E_g)^p$. Where P is a constant that relies on the kind of the electronic transitions. P is equal to ½ for allowed direct transition. Also, P may be equivalent to 3/2 for forbidden direct transition, 2 for indirect allowed transition, and 3 for indirect forbidden transitions. A is a constant, the Plank's constant is h.

ZnO has a big exciton binding energy of 60 MeV, also is a hexagonal wurtzite crystal structure semiconductor, and has a direct large band gap of 3.37 eV [25, 26]. We got the optical band gap through charting $(\alpha h\nu)^2$ as a function of photon energy (hν). We draw multi plots of $(\alpha h\nu)^2$ as a function of (hν) for ZTF, Z15FTF, Z20FTF, Z25FTF, and Z30FTF, respectively as displayed in Fig.5. The values of the

As displayed in Fig. 4, the ZTF and Z25FTF elemental components were investigated using electron dispersive x-ray spectroscopy (EDX). The position of the peaks in a typical EDX spectrum verifies the existence of the main elements. However, the peak altitude aids in quantifying the elemental concentration of each sample [23]. Fig. 3(a) shows the EDX result of the undoped ZnO material, which confirms the existence of zinc and oxygen by a larger intensity peak of zinc, while Fig. 3(b) shows evidence of the existence of iron for the doped sample.

direct energy gap Eg were obtained by the interrupt of the extrapolation to zero absorption with photon energy axis. It is clear that the direct energy gap increases by increasing iron concentrations until Z25FTF and then it decreases at Z30FTF. The obtained results indicated that the energy band gap of ZTF, Z15FTF, Z20FTF, Z25FTF and Z30FTF are 3.138, 3.234, 3.240, 3.242, 2.936eV , respectively.

Fig. 4(b) presents the transmittance diagram of ZTF, Z15FTF, Z20FTF, Z25FTF and Z30FTF, respectively. The transmittance (T %) of the samples was reduced in the UV region and raised by increasing the wavelength until the Near Infrared region of the
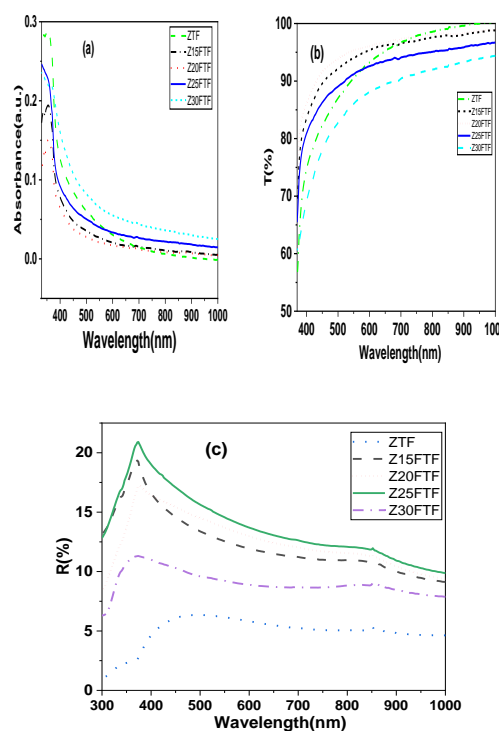

Fig. 4(a) The absorbance spectrum (A) , (b) The Transmittance spectrum (T%) and (c) The Reflectance spectrum (R%)for ZTF , Z15FTF,Z20FTF,Z25FTF and Z30FTF,respectively ,sintered for 2 hours at 500 ^{0}C.

_____

electromagnetic spectrum. The T% of ZTF film showed an average value of nearly 97% and decreased by increasing the Fe concentrations. The reduction in T% of ZnO after adding Fe-dopant might be owing to the improved grain boundaries as a result of decreasing the crystallite sizes [27]. These films may be used to galvanize a variety of substance surfaces because of their ability to protect substance surfaces from oxidization.

Fig. 4(c) indicates the reflectance charts of the prepared samples. The samples had the highest reflectance value at around 21% in the Ultraviolet-visible region of the electromagnetic spectrum, which decreased as the wavelength increased.

Fig. 5(a) demonstrates the plot of α versus hv. The extinction coefficient k, which evaluates the lost quantity of light when scattering and absorption per unit distance of the penetration medium happens [29] and is presented in equation (11) as ;

$$K= \frac{\alpha \lambda}{4 \pi} \qquad (11)$$

Where λ is the wavelength. As mentioned by Nwofe and Agbo [30], the refractive index, n is calculated from equation (12);

$$n= \frac{1+R^{1/2}}{1-R^{1/2}} \qquad (12)$$

Fig. 6(a) and (b) presents n and k versus photon energy charts for ZTF, Z15FTF, Z20FTF, Z25FTF and Z30FTF, respectively.

In Fig. 6(b), k increases by increasing the photon energy for all the prepared materials. When compared to the other samples, the Z30FTF had high k values. For samples with high Fe concentrations, an increase in k value can be related to a reduction in T % and an increase in α. These films could be very beneficial in the production of solar cells.

Fig. 6(a) revealed that the n was reduced by rising the photon energy which, indicated similar dispersion behavior of the samples. Optical conductivity (σ0) is determined by the equation's relationship (13) [31] which is the optical reaction of a transparent material.

$$\sigma_0 = \frac{\alpha c n}{4 \pi} \qquad (13)$$

Where c=3*10^8 m/s, the speed of light. The graph of σ0 against hv for ZTF, Z15FTF, Z20FTF, Z25FTF, and Z30FTF is displayed in Fig. 7(c). From Fig. 7(c), optical conductivity, σ0 enlarged by an elevation in hv for all the samples. We detected that increasing the iron concentration in Z30FTF has a significant impact on the materials' optical conductivity.

The permittivity (ε= ε_r+ jε_i) is split into two portions: the real permittivity (ε_r), which measures the bridging of the speed of light within the material and the imaginary permittivity (ε_i) measures the absorption of

the energy from the electric field by the dielectric material due to dipole movement. the real permittivity part was plotted using equation (14), while the imaginary permittivity part was plotted using equation (15) [32]:

$$\varepsilon_r = n^2 + k^2 \qquad (14)$$
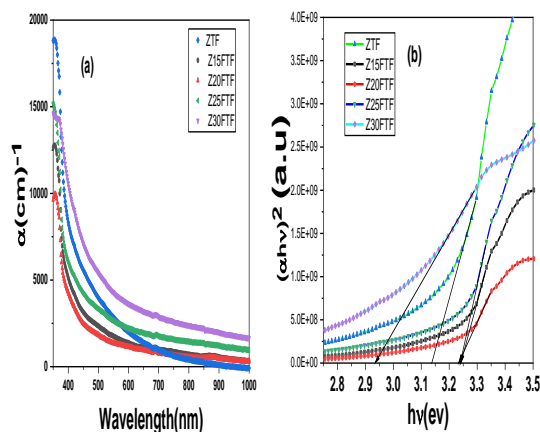
$$\varepsilon_i = 2nk \qquad (15)$$

Fig.5 The absorption coefficient (α) (a) and (αhv)^2 as a function of photon energy (b) for ZTF, Z15FTF, Z20FTF, Z25FTF and Z30FTF, respectively, sintered at 500 ^{0}C for 2 hours.

Fig. 7(a and b) display graphs of real and imaginary permittivity versus hv; the real permittivity part is associated with the refractive index thanks to the very small value of k^2 compared to n^2, whilst the imaginary permittivity part is dependent on k and n also.

The real permittivity values are elevated than the imaginary permittivity values in this study. It is shown from Fig. 7(a) that all the samples' real permittivity has the same behavior, they decrease by increasing photon energy until 1.4 eV, and afterward dramatically increase while photon energy rises. the imaginary permittivity illustrated in Fig. 7(b) rises while photon energy increases.

The addition of Fe dopant increased the energy band gap of ZnO as a consequence of the excess concentration of carriers in the conduction band of ZnO. The energy band gap is reduced as a result of the interaction between free carriers caused by a high concentration of Fe, as shown in Fig. 5(b). The band bending effect caused by stress in films is responsible for the remarked blue shift in the band gap for the prepared films. With an increase in iron concentration, the system shifts from expansive to compressive stress. A large band gap is expected [33], owing to the high repulsion in the compressed lattice between the oxygen 2p and zinc 4s bands.
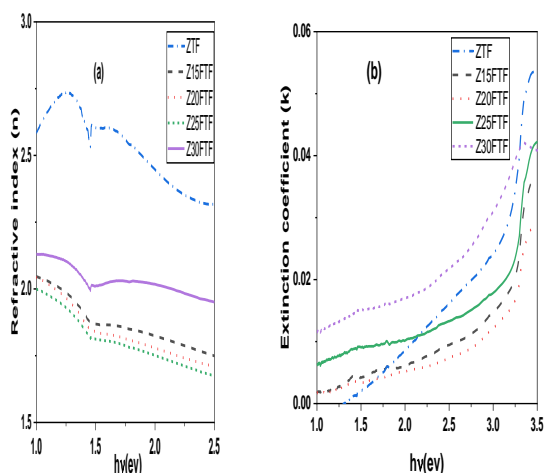
_____

Fig. 6 The refractive index (a)and the extinction coefficient (b) for ZTF, Z15FTF, Z20FTF, Z25FTF and Z30FTF, respectively, sintered at 500 ^{0}C for 2 hours.
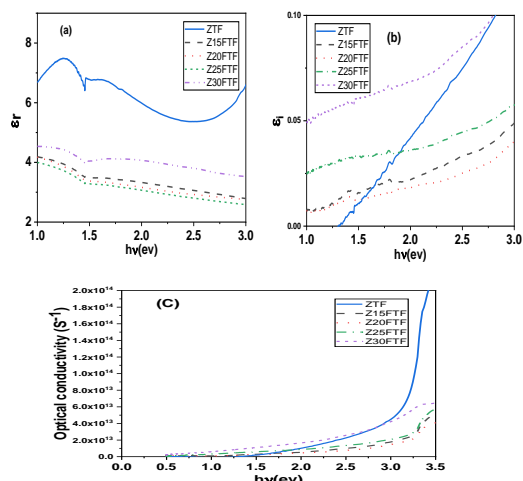

Fig.7 (a) real, (b) imaginary dielectric constants and (c) the optical conductivity for ZTF, Z15FTF, Z20FTF, Z25FTF and Z30FTF, respectively,

4. Conclusions

Pure and iron-doped ZnO nano-structure thin films with various concentrations; ZTF, Z15FTF, Z20FTF, Z25FTF, and Z30FTF were well prepared by the modified spin coating sol-gel technique. The wurtzite hexagonal structure prepared samples to decrease in intensity by increasing the iron content as a result of replacing the Zn^{+2} (AN=30) with the lower value of Fe (AN=26). It is seen in the Raman spectra of pure and doped ZnO that there is one mode at 440 cm^{-1} (E_2high) and a broadband mode centred at 562 cm^{-1} A_1(TO) component. The EDX analysis found that the film's composition is nearly stoichiometric. Iron doping has a major influence on the morphology of doped films, as indicated by FESEM micrographs. More adding of

iron reduces the pores present in pure films. The direct energy gap widens as doping concentrations raise until Z25FTF, then shrink until Z30FTF. The obtained results indicated that the energy band gap of ZTF, Z15FTF, Z20FTF, Z25FTF, and Z30FTF are 3.138, 3.234, 3.240, 3.242, 2.936eV, respectively, owing to hybridization of dopants with ZnO. As doping concentrations rise, the refractive indices decrease until Z25FTF, then rise at Z30FTF.

5. Conflict of Interest:
The authors declare that there is no conflict of interest

6. References

[1] Pietrzyk, M. A., Zielony, E., Stachowicz, M., Reszka, A., Płaczek-Popko, E., Wierzbicka, A., Przezdziecka, E., Droba, A., & Kozanecki, A. (2014). Electro-optical characterization of ZnO/ZnMgO structure grown on p-type Si (111) by PA-MBE method. *Journal of Alloys and Compounds*, *587*, 724–728.

[2] Saito, N., Haneda, H., Sekiguchi, T., Ohashi, N., Sakaguchi, I., & Koumoto, K. (2002). Low-Temperature Fabrication of Light-Emitting Zinc Oxide Micropatterns Using Self-Assembled Monolayers. *Advanced Materials*, *14*(6), 418–421.

[3] Liang, S., Sheng, H., Liu, Y., Huo, Z., Lu, Y., & Shen, H. (2001). ZnO Schottky ultraviolet photodetectors. *Journal of Crystal Growth*, *225*(2-4), 110–113.

[4] Kluth, O., Schöpe, G., Hüpkes, J., Agashe, C., Müller, J., & Rech, B. (2003). Modified Thornton model for magnetron sputtered zinc oxide: film structure and etching behavior. *Thin Solid Films*, *442*(1-2), 80–85.

[5] Huang, M. H. (2001). Room - Temperature Ultraviolet Nanowire Nanolasers. Science, 292(5523), 1897–1899.

[6] Zou, Z., Ye, J., Sayama, K., & Arakawa, H. (2001). Direct splitting of water under visible light irradiation with an oxide semiconductor photocatalyst. *Nature*, *414*(6864), 625–627.

[7] Shishiyanu, S. T., Shishiyanu, T. S., & Lupan, O. I. (2005). Sensing characteristics of tin doped ZnO thin films as NO2 gas sensor. *Sensors and Actuators B: Chemical*, *107*(1), 379–386.

[8] Cui, M. L., Wu, X. M., Zhuge, L. J., & Meng, Y. D. (2008). Growth of fractal patterns in ZnO films doped with Fe. *Vacuum*, *82*(6), 613–616.

_____

[9] Yılmaz, S., McGlynn, E., Bacaksız, E., Cullen, J., & Chellappan, R. K. (2012). Structural, optical, and magnetic properties of Ni-doped ZnO micro-rods grown by the spray pyrolysis method. *Chemical Physics Letters*, *525-526*, 72–76.

[10] Wang, A., Zhong, Z., Lu, C., Lv, L., Wang, X., & Zhang, B. (2011). Study on field-emission characteristics of electrodeposited Co-doped ZnO thin films. *Physica B: Condensed Matter*, *406*(5), 1049–1052.

[11] An, X., Hu, D., Li, H., Li, L., Chong, X., & Wang, Y. (2011). Nanostructure and optical properties of M doped ZnO (M=Ni, Mn) thin films prepared by Sol-gel process. *Physica B: Condensed Matter*, *406*(20), 3956-3962.

[12] Singh, K., Devi, V., Dhar, R., & Mohan, D. (2015). Structural, optical, and electronic properties of FE doped ZnO thin films. *Superlattices and Microstructures*, *85*, 433-437.

[13] Miao, Y., Ye, Z., Xu, W., Chen, F., Zhou, X., Zhao, B., Zhu, L., & Lu, J. (2006). P-Type conduction in phosphorus-doped ZnO thin films by MOCVD and thermal activation of the dopant. *Applied Surface Science*, *252*(22), 7953-7956.

[14] Dhanalakshmi, A., Thanikaikarasan, S., & Natarajan, B. (2017). Influence of Mn dopant concentration on film thickness, structural, morphological, compositional, and optical properties of zinc oxide thin films. *Journal of Materials Science: Materials in Electronics*, *28*(16), 11576-11583.

[15] Shaban, M., & El Sayed, A. (2015). Influences of lead and magnesium Co-doping on the nano structural, optical properties, and wettability of spin-coated zinc oxide films. *Materials Science in Semiconductor Processing*, *39*, 136-147.

[16] Patterson, A. L. (1939). The Scherrer formula for X-ray particle size determination. *Physical Review*, *56*(10), 978-982.

[17] Cherifi, Y., Chaouchi, A., Lorgoilloux, Y., Rguiti, M., Kadri, A., & Courtois, C. (2016). Electrical, dielectric, and photocatalytic properties of FE-doped ZnO nanomaterials synthesized by Sol-gel method. *Processing and Application of Ceramics*, *10*(3), 125-135.

[18] Mishra, A., & Das, D. (2010). Investigation on Fe-doped ZnO nanostructures prepared by a chemical route. *Materials Science and Engineering: B*, *171*(1-3), 5-10.

[19] Srinivasulu, T., Saritha, K., & Reddy, K. R. (2017). Synthesis and characterization of FE-doped ZnO thin films deposited by chemical spray pyrolysis. *Modern Electronic Materials*, *3*(2), 76-85.

[20] Ghanem, M. G., Badr, Y., Hameed, T. A., El Marssi, M., Lahmar, A., Wahab, H. A., & Battisha, I. K. (2019). Synthesis and characterization of undoped and Er-doped ZnO nano-structure thin films deposited by Sol-gel spin coating technique. *Materials Research Express*, *6*(8), 085916.

[21] SILAMBARASAN, M., SARAVANAN, S., OHTANI, N., & SOGA, T. (2014). Raman and Photoluminescence Studies of Ag and Fe-doped ZnO Nanoparticles.Int.J. ChemTech Res,7(3) ,1644-1650.

[22] Yahia, S. B., Znaidi, L., Kanaev, A., & Petitet, J. (2008). Raman study of oriented ZnO thin films deposited by Sol-gel method. *Spectrochimica Acta Part A: Molecular and Biomolecular Spectroscopy*, *71*(4), 1234-1238.

[23] Pal Singh, R. P., Hudiara, I., & Bhushan Rana, S. (2016). Effect of calcination temperature on the structural, optical, and magnetic properties of pure and FE-doped ZnO nanoparticles. *Materials Science-Poland*, *34*(2), 451-459.

[24] Nkele, A. C., Nwanya, A. C., Nwankwo, N. U., Osuji, R. U., Ekwealor, A. B., Ejikeme, P. M., Maaza, M., & Ezema, F. I. (2019). Investigating the properties of nano nest-like nickel oxide and the NIO/Perovskite for potential application as a hole transport material. *Advances in Natural Sciences: Nanoscience and Nanotechnology*, *10*(4), 045009.

[25] Hacini, N., Ghamnia, M., Dahamni, M. A., Boukhachem, A., Pireaux, J., & Houssiau, L. (2021). Compositional, structural, morphological, and optical properties of ZnO thin films prepared by PECVD technique. *Coatings*, *11*(2), 202.

[26] Wahab, H., Salama, A., El-Saeid, A., Nur, O., Willander, M., & Battisha, I. (2013). Optical, structural, and morphological studies of (ZnO) nano-rod thin films for biosensor applications using the Sol-gel technique. *Results in Physics*, *3*, 46-51.

[27] OriakuCI and Osuwa JC2009 On the optical dispersion parameters of thin-film Al 3 doped

_____

ZnO transparent conducting glasses Journal of Ovonic Research 5 213–218.

[28] Abdulrahman, A. F., Ahmed, S. M., Hamad, S. M., & Barzinjy, A. A. (2021). Effect of growth temperature on morphological, structural, and optical properties of ZnO Nanorods using modified chemical bath deposition method. *Journal of Electronic Materials*, *50*(3), 1482-1495.

[29] Aslan, E., & Zarbali, M. (2022). Tuning of photosensitivity and optical parameters of ZnO-based photodetectors by Co-sn and ti doping. *Optical Materials*, *125*, 112030.

[30] Agbo P E and Nwofe P A (2015). Comprehensive studies on the optical properties of ZnO-core–shell thin films J. Nanotechnol. Adv. Mater 3 63–97.

[31] Ikhioya, I. L., Akpu, N. I., & Nkele, A. C. (2021). Influence of ytterbium (Yb) dopant on the optical properties of electrochemically deposited zinc oxide (ZnO) films. *Materials Research Express*, *8*(1), 016403.

[32] Najm, S. S. (2021). Doping effect on the optical properties of (PVA: ZNO) nanocomposites. *Materials Today: Proceedings*.

[33] Kumari, V., Kumar, V., Malik, B. P., Mehra, R. M., & Mohan, D. (2012). Nonlinear optical properties of erbium doped zinc oxide (EZO) thin films. *Optics Communications*, *285*(8), 2182–2188.

_____

Egypt. J. Chem..**65,**, No. SI:13B (2022)